Interfacial Charge Transfer and Transport in Polyacetylene-Based Heteroionic Junctions: Quantum Chemistry Calculations and Molecular Dynamics Simulations

Hui Cao, Tao Fang, Shuhua Li, and Jing Ma*

School of Chemistry and Chemical Engineering, Institute of Theoretical and Computational Chemistry, Key Laboratory of Mesoscopic Chemistry of MOE, Nanjing University, Nanjing, 210093, People's Republic of China

Received February 13, 2007; Revised Manuscript Received March 29, 2007

ABSTRACT: A theoretical description of the heteroionic junction Au|$\mathbf{P_C}$|$\mathbf{P_A}$|Au (poly(tetramethylammonium 2-cyclooctatetraenylethanesulfonate) ($\mathbf{P_A}$), poly[(2-cyclooctatetraenylethyl) trimethylammonium trifluoromethanesulfonate] ($\mathbf{P_C}$)) is presented on the basis of the relative energy levels of its components and the characteristics of each interface in the device. Electronic structures of ionically functionalized polyacetylene analogues, $\mathbf{P_A}$ and $\mathbf{P_C}$, are surveyed by both oligomer investigations (using density functional theory with the aid of an effective linear scaling strategy) and polymer calculations (with the periodic boundary condition). The solvent effects on the band edges of $\mathbf{P_A}$ and $\mathbf{P_C}$ in the solvent of acetonitrile are also estimated by using both the polarizable continuum model (PCM) and the explicit solvent model. The absence of n-doping wave of the $\mathbf{P_A}$ observed experimentally is attributed to its high conductance band edge (−2.71V vs SCE in gas phase and about −2.17V vs SCE in solvent of acetonitrile) or the breakdown of effective interfacial electron transfer. The reported unidirectional transport behavior of Au|$\mathbf{P_C}$|$\mathbf{P_A}$|Au junctions is rationalized on the basis of analyses of electron transfer between $\mathbf{P_A}$ and Au electrode and electron tunneling at the $\mathbf{P_C}$|$\mathbf{P_A}$ interface.

1. Introduction

Transport involving both the electronic and ionic processes is a fascinating subject in fabrication of microelectronic devices, such as light-emitting electrochemical cells (LECs),[1−3] electrochemical transistors,[4−6] and electric current rectifiers.[7−9] In such devices, the salts, introduced into the active materials sandwiched between two electrodes, provide the counterions and facilitate the formation of dynamic and reversible electrochemical doping under external bias. Mobile ions may improve the injection of electrons and holes from electrodes to the polymer layer. The height and thickness of the barrier at the polymer/electrode interface as well as the bulk transport behaviors are changed due to the voltage-induced ion redistributions when external bias is applied. Different from the pure electronic conduction in the light-emitting diodes (LEDs)[10−12] with the pristine polymer, e.g., poly(1,4-phenylenevinylene) (PPV) and its derivatives, ions play an important role in the mixed electronic/ionic transport process, which stimulates intensive explorations of the potential utilization of the ions incorporated conjugated polymers in electronic devices.

Recently, Lonergan and co-workers have carried out pioneer studies on the ionically functionalized polyacetylene analogues, poly(tetramethylammonium 2-cyclooctatetraenylethanesulfonate) ($\mathbf{P_A}$) and poly[(2-cyclooctatetraenylethyl)trimethylammonium trifluoromethanesulfonate] ($\mathbf{P_C}$) (shown in Scheme 1),[8,9,13−16] which are two single-component systems of mixed electronic/ionic conductors in contrast to those ordinary blends of conjugated polymers and the polymer electrolytes.[1−3] Single-electrode voltammetry data for ∼1.5 μm film of $\mathbf{P_C}$ or $\mathbf{P_A}$ on the glassy carbon electrode in 0.075 M Me_4NBF_4/CH_3CN have shown that the potential corresponding to the n-doping of $\mathbf{P_C}$ is −1.04V vs the saturated calomel electrode (SCE), and the p-doping potentials of $\mathbf{P_A}$ and $\mathbf{P_C}$ are 0.30 and 0.40 V vs SCE, respectively.[13] Although $\mathbf{P_A}$ and $\mathbf{P_C}$ have nearly identical UV/vis absorption spectra, the absence of the n-doping wave for $\mathbf{P_A}$ (in solution of 0.075 M Me_4NBF_4/CH_3CN) to potentials as reducing as −1.5 V vs SCE[13] is not yet well understood. On the basis of the fabrication of $\mathbf{P_C}$|$\mathbf{P_A}$ bilayer, Lonergan and co-workers reported an unidirectional current behavior of the heteroionic junction in the Au|$\mathbf{P_C}$|$\mathbf{P_A}$|Au junction (shown in Scheme 1), which was ascribed to the asymmetry in ion polarization processes at Au|$\mathbf{P_C}$ and $\mathbf{P_A}$|Au interfaces.[8] Nevertheless, electronic structures of the polymer/polymer interface, $\mathbf{P_C}$|$\mathbf{P_A}$, may also control these current−voltage response behaviors, sparkling off our present theoretical study on the structure and properties of all the involved interfaces in the Au|$\mathbf{P_C}$|$\mathbf{P_A}$|Au junction.

Scheme 1. Au|$\mathbf{P_C}$|$\mathbf{P_A}$|Au Junction with the Ionically Functionalized Polyacetylene Analogues, $\mathbf{P_C}$ and $\mathbf{P_A}$, Sandwiched between Two Au Electrodes

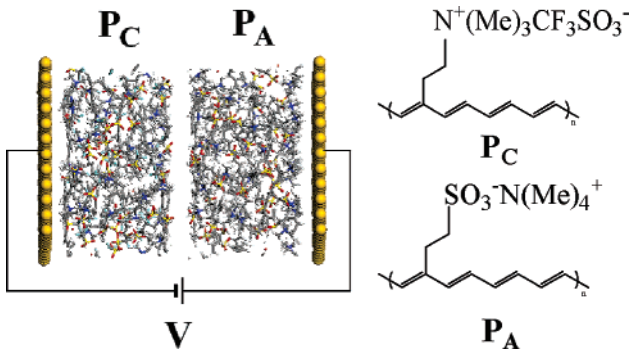

Although molecular wire junctions based on low molecular weight materials[17] such as benzene dithiol, alkane dithiol, and oligophenylene ethynylene dithiol, etc., and polymer molecular junctions comprising Au nanoparticles and conjugated polymers[18] have been intensively investigated, few theoretical works have been reported on such polyacetylene-based heteroionic junction due to complications involving with polymer/electrode and polymer/polymer interfaces. Aroused by the successful

* Corresponding author. E-mail: majing@netra.nju.edu.cn.

10.1021/ma0703857 CCC: $37.00
Published on Web 05/16/2007

Table 1. Total Energies (in Units of au) Calculated by EC-MFCC Scheme and the Conventional B3LYP Method with the Basis Set of 6-31G(d)

oligomer	EC-MFCC	conventional
***n*P$_A$**		
$n = 2$	−2452.853 753	−2452.854 122
$n = 3$	−3678.692 956	−3678.693 715
***n*P$_C$**		
$n = 2$	−3048.253 962	−3048.254 717
$n = 3$	−4571.792 618	−4571.792 754

realization of this polyacetylene-based junction as well as interesting problems concerning the underlying mechanism of transport of carriers, here we attempt to understand the unusual transport properties of the Au|**P$_C$**|**P$_A$**|Au junction by employing both quantum chemistry calculations and molecular dynamics (MD) simulations.

Density functional theory (DFT) is a practical tool for studying the ground state properties of the π-conjugated oligomers and polymers. However, it is still a challenge to investigate the electronic structures of macromolecules with thousands of basis functions, since the computational cost increases exponentially ($O(N^\alpha)$, $\alpha \geq 3$) with the system size. Fortunately, various fragment-based linear scaling approaches ($O(N)$) have been developed.[19−23]Among them, the energy-corrected molecular fractionation with conjugated caps (EC-MFCC) method has been demonstrated to be capable of predicting with high accuracy both ground-state energies and optimized geometries of very large molecules at the ab initio level.[23] Therefore, we employ the EC-MFCC scheme within the framework of DFT to optimize the structures of the ionically functionalized oligomers, ***n*P$_A$** and ***n*P$_C$** with up to eight units ($n = 1-8$). Both the oligomer extrapolation from the highest occupied molecular orbital (HOMO) and the lowest unoccupied molecular orbital (LUMO) energy levels and the periodic boundary condition (PBC) calculations are adopted to gain a comprehensive understanding of the band structures of **P$_A$** and **P$_C$**. Solvent effects that cause the upshift or downshift in the band edges of **P$_A$** and **P$_C$** are also taken into account by both the polarizable continuum model (PCM) and explicit solvent model incorporating MD simulations and DFT calculations.

In this work, the absence of n-doping wave of **P$_A$** in solution of 0.075 M Me_4NBF_4/CH_3CN observed experimentally is rationalized, and we give a qualitative picture in elucidating interesting phenomena shown in the charge transfer and transport process in the Au|**P$_C$**|**P$_A$**|Au junction. Our theoretical results reported herein may shed light on the future design of novel polymer-based junctions and understanding of other conduction phenomena such as the surface transfer doping of semiconductors.[24]

2. Computational Details

Quantum Chemistry Calculations. As mentioned above, we will employ the EC-MFCC scheme within the framework of DFT theory (specifically, B3LYP[25−27]) to optimize the geometries of ***n*P$_A$** and ***n*P$_C$** ($n = 4-8$) oligomers. The computational details of the EC-MFCC method for the studied systems are given in Supporting Information (Figure S1). At the EC-MFCC optimized structures, conventional single-point B3LYP/6-31G(d) calculations are carried out with the Gaussian 03 program[28] to obtain energy levels of HOMOs and LUMOs of ***n*P$_A$** and ***n*P$_C$**.

In order to test the performance of the EC-MFCC scheme, we have collected in Table 1 the total energies of short oligomers ***n*P$_A$** and ***n*P$_C$** ($n = 2-3$) calculated with the EC-MFCC and conventional approaches at their respective optimized geometries. One can see that the total energies calculated by the EC-MFCC scheme are in good agreement with those from conventional calculations. In addition, the optimized structures obtained by the conventional and EC-MFCC schemes are also very close to each other. In fact, the HOMO and LUMO energy levels calculated at the EC-MFCC-B3LYP/6-31G(d) geometry differ from those at the B3LYP/6-31G(d) geometry only by less than 0.01 eV. On the basis of these results, the EC-MFCC scheme will be used to optimize the geometries of longer oligomers (up to 8 units), which are beyond the scope of conventional DFT calculations. The band edges of the corresponding polymers are hence estimated by the oligomer extrapolation method from the HOMO and LUMO energy levels of oligomers, as done in the literature.[29−32]

Energy Band Calculations. Band structures are calculated with the CASTEP program in the *Cerius*^{2} package[33] using the DFT method with plane wave basis sets. PW91 functional and Ultrasoft pseudopotential are applied, and the cutoff energy of plane waves is set to be 260.0 eV.

The original unit cells are set to be 9.6 Å × 30.0 Å × 20.0 Å for both **P$_A$** and **P$_C$**. Geometries of the repeated units and cells are simultaneously optimized, and then the band structures are calculated accordingly.

Solvent Models. Two kinds of solvent models,[34] the polarizable continuum model (PCM) and the explicit solvent model, are adopted to investigate the influences of CH_3CN solvent molecules (chosen according to the experimental conditions in ref 13) on the energy levels of the frontier orbitals of ***n*P$_A$** and ***n*P$_C$**. In PCM calculations, we only obtain the optimized geometries of **1P$_A$** and **1P$_C$** in the background of an electrostatic field with $\epsilon = 36.64$, while optimizations of higher oligomers are rather computationally expensive under the present condition. Hence, we resort to the explicit solvent model within the framework of a combined MD and DFT treatment. All MD simulations are performed in NVT ensemble with systems maintained at 298 K. Equations of motion for systems are integrated using the velocity Verlet algorithm[35] with the time step of 1 fs. Here, a 41.00 Å × 41.00 Å × 43.21 Å amorphous unit cell filled with one ***n*P$_A$** or ***n*P$_C$** ($n = 1, 2$) solute molecule surrounded by 800 CH_3CN molecules is constructed. The gas-phase geometries of ***n*P$_A$** or ***n*P$_C$** optimized from B3LYP/6-31G(d) calculations are directly applied in MD simulations, since almost all the available force fields cannot describe the alternation of single and double bonds in backbones of polyacetylene very well. In all MD simulations, the force field of pcff is applied. After the MD simulations, a cluster model of solvated ***n*P$_A$** or ***n*P$_C$** oligomer, consisting of about 70 CH_3CN molecules in vicinity to the solute within the range of 5 Å, is used as the input in the DFT single point calculations. The final results for analysis are based on the average values of 10 configurations, which are taken out per 5 ps over the whole 50 ps simulations. In fact, such a strategy has been extensively employed in the treatments of liquids (e.g., water) and solutions.

3. Results and Discussion

3.1. Geometries of *n*P$_A$ and *n*P$_C$ Oligomers. Polyacetylene (**PA**) has evoked considerable theoretical interests[36] since the discovery of its metallic electrical conductivity after oxidatively doping in the late 1970s.[37,38] However, few theoretical investigations have been carried out on the ionically functionalized polyacetylene analogues, **P$_C$** and **P$_A$**, to date. Hence, it is interesting to survey differences in electronic structures between these ionically functionalized species (**P$_C$**, **P$_A$**) and the parent system of *trans*-polyacetylene (***t*-PA**). The geometries of oli-

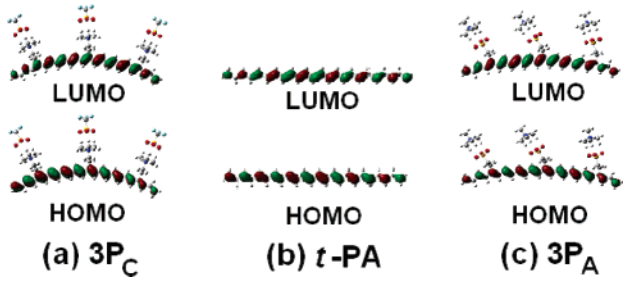

Figure 1. Optimized geometries along with the HOMO and LUMO orbitals of (a) **3P$_C$**, (b) ***t*-PA** (containing the same number of carbon atoms in the backbone as those of **3P$_A$** and **3P$_C$**), and (c) **3P$_A$** on the basis of B3LYP/6-31G(d) calculations.

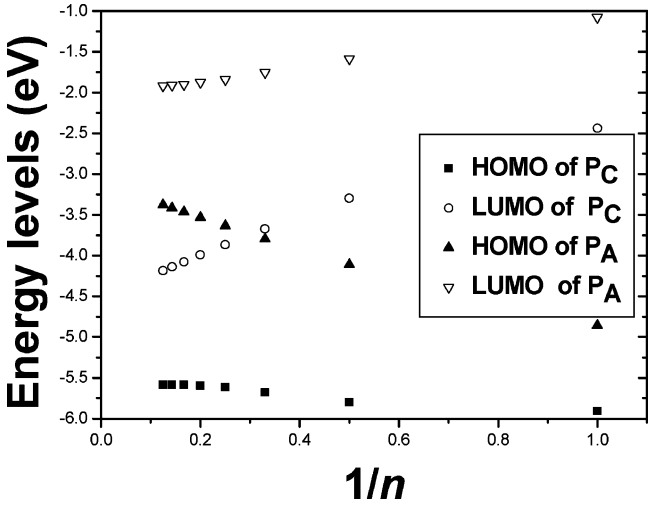

Figure 2. HOMO and LUMO energy levels of ***n*P$_A$** and ***n*P$_C$** oligomers as a function of 1/*n*, where *n* is the number of the repeating units along the polymer chain. Energy levels are calculated at the level of B3LYP/6-13G(d).

gomer chains of ***n*P$_C$** and ***n*P$_A$** (with up to $n = 8$), in predominately *trans* form,[14,15] are fully optimized by the EC-MFCC method within the framwork of B3LYP/6-31G(d). Compared with the linear ***t*-PA**, oligomers of ***n*P$_C$** and ***n*P$_A$** have different degrees of bending in their backbones, as illustrated by the optimized geometries of **3P$_C$**, **3P$_A$**, and dodecaacetylene in Figure 1. (The optimized structures of other oligomers of **P$_A$** and **P$_C$** are shown in Figure S2 of the Supporting Information.) The anionic side chain $-C_2H_4SO_3^-$ leans to the backbone of ***n*P$_A$** chain, whereas the cationic side group, $-C_2H_4N(Me)_3^+$, of **P$_C$** is nearly perpendicular to the carbon chain. It seems that in **P$_A$** one of the oxygen atoms of the $-C_2H_4SO_3^-$ group forms a weak intramolecular interaction with the nearby hydrogen atom on the carbon chain; for **P$_C$**, because of the large steric hindrance around the nitrogen atom in the $-C_2H_4N(Me)_3^+$ group, it is impossible for the nitrogen atom to interact directly with hydrogen atoms on the backbone. In spite of the bending structures, the conjugation of π-electrons along their carbon backbones still maintains well, as reflected from similar values of the bond length alternations (BLAs) along the main backbone, 0.072 and 0.071 Å in **3P$_C$** and **3P$_A$**, respectively, to that in dodecaacetylene (0.070 Å).

3.2. Band Edges of Ionically Functionalized Polymers. In order to investigate the electronic structures of **P$_A$** and **P$_C$**, both the oligomer extrapolation strategy and the energy band calculation with the translational symmetry are employed in the present work.

Oligomer Extrapolations in the Gas Phase. According to the B3LYP/6-31G(d) calculation results, shown in Table 2, we find that there is a good linear relationship between the HOMO (LUMO) energy levels of ***n*P$_A$** (***n*P$_C$**) and the corresponding reciprocal number of their repeating units, 1/*n*, as shown in Figure 2. HOMO and LUMO energy levels of these oligomers are extrapolated to get the valence band (VB) and conduction band (CB) edges of **P$_A$** (**P$_C$**) of −3.12 eV (−5.52 eV) and −2.03 eV (−4.50 eV), respectively (Table 2). In fact, the B3PW91/6-31G(d) calculations give nearly the same results with the deviations within about 0.1 eV.

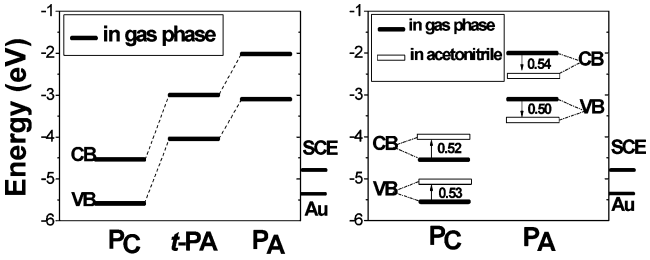

(a) Shift by functionalization **(b) Shift by solvents**

Figure 3. Influences of (a) side chains of **P$_A$** and **P$_C$** on band edges ralative to the parent system of *trans*-polyacetylene (***t*-PA**) and (b) the solvent of acetonitrile on band edges of **P$_A$** and **P$_C$**. The VB and CB edges of anionically functionalized **P$_A$** shift up, whereas those of cationically functionalized **P$_C$** shift down relative to those of ***t*-PA**. The CH_3CN solvent molecules cause the upshift of band edges in **P$_C$** and the downshift in **P$_A$**. The chemical potentials of SCE and Au are also shown for comparison.

It can be also found from Table 2 and Figure 3a that the VB and CB edges of anionically functionalized **P$_A$** shift up, whereas those of cationically functionalized **P$_C$** shift down in comparison with those of ***t*-PA**. Obviously, the different side chains of **P$_A$** and **P$_C$** cause the reverse band shifts relative to ***t*-PA**. The local charges carried by the $-C_2H_4N(Me)_3^+$ or $-C_2H_4SO_3^-$ may play a dominant role in shifting the band edges of **P$_A$** and **P$_C$** relative to ***t*-PA**, since the HOMO and LUMO of ***n*P$_A$** and ***n*P$_C$** are largely localized along the backbone, as exemplified by **3P$_A$** and **3P$_C$** in Figure 1. The shift of band edge was considered as the result of the interaction between the electrons on the energy band and the charges on the side chains.[39−41] The energy of the electrons on the VB rises up (or lowers down) due to the repulsion (or attraction) by the negatively (or positively) charged side chains. Thus, the energy band of **P$_A$** (or **P$_C$**) shifts upward (or lowers down). In fact, a band shift of about 0.5 eV was also observed in single-walled carbon nanotubes encapsulating potassium.[42] Similarly, shifts of band edges of other π-conjugated polymers such as polythiophene, polypyrrole, and polyphenylene, etc., upon the modifications of side chains have been reported.[43,44]

We can determine the relative positions of the band edges of **P$_A$** and **P$_C$** to the chemical potential of SCE. The normal chemical potential of hydrogen electrode is −4.50 eV vs vacuum.[45]According to this conversion relationship between the redox potential and the chemical potential, it can be deduced that the value of the chemical potential of SCE is −4.74 eV. It can be found from Table 2 and Figure 3a that the chemical potential of SCE lies between the VB edge (−5.52 eV) and CB edge (−4.50 eV) of **P$_C$**, whereas it is below the VB edge (−3.12 eV) and CB edge (−2.03 eV) of **P$_A$**. However, the observed *onset* potential of p-doping process of **P$_A$** is about −0.40V vs SCE (i.e., −4.34 eV), and those of the p- and n-doping processes of **P$_C$** are about 0.20 and −0.90 V vs SCE (i.e., −4.94 and −3.84 eV), respectively. Therefore, the calculated VB (CB) edge of **P$_C$** in gas phase is underestimated by about 0.58 eV (0.66 eV) relative to the electrochemical experimental data measured in 0.075 M Me_4NBF_4/CH_3CN dilute

Table 2. HOMO (LUMO) Energies in Gas Phase and the Solvent of Acetonitrile (CH_3CN), HOMO−LUMO Gaps (Δ_{H-L}) in Gas Phase, Calculated at the Level of B3LYP/6-31G(d) (in Units of eV); Experimental Band Gaps of *t*-PA, P_A, and P_C Are Given for Comparison

	in gas phase		HOMO (LUMO) in acetonitrile		band gap	
system	HOMO (LUMO)	Δ_{H-L}	explicit model	PCM	theor[a]	expt
***t*-PA**						
$n = 1$	−5.36 (−1.57)	3.79				
$n = 2$	−4.75 (−2.23)	2.52				
$n = 3$	−4.51 (−2.48)	2.03				
$n = 4$	−4.39 (−2.61)	1.78				
$n = 5$	−4.31 (−2.69)	1.62				
$n = 6$	−4.26 (−2.74)	1.52				
$n = 7$	−4.22 (−2.78)	1.44				
$n = 8$	−4.20 (−2.80)	1.40				
$n = \infty$	−4.01 (−3.00)				1.01	1.48[b]
P_A						
$n = 1$	−4.85 (−1.07)	3.78	−5.41 (−1.69)	−5.31 (−1.53)		
$n = 2$	−4.11 (−1.58)	2.53	−4.61 (−2.12)			
$n = 3$	−3.80 (−1.75)	2.04				
$n = 4$	−3.63 (−1.84)	1.79				
$n = 5$	−3.53 (−1.87)	1.66				
$n = 6$	−3.46 (−1.89)	1.57				
$n = 7$	−3.41 (−1.91)	1.50				
$n = 8$	−3.38 (−1.91)	1.47				
$n = \infty$	−3.12 (−2.03)		−3.62 (−2.57)		1.09 (1.05)	
P_C						
$n = 1$	−5.91 (−2.44)	3.48	−5.90 (−2.24)	−5.54 (−1.77)		
$n = 2$	−5.80 (−3.30)	2.51	−5.27 (−2.78)			
$n = 3$	−5.68 (−3.67)	2.01				
$n = 4$	−5.61 (−3.86)	1.75				
$n = 5$	−5.59 (−3.99)	1.60				
$n = 6$	−5.58 (−4.07)	1.51				
$n = 7$	−5.58 (−4.14)	1.44				
$n = 8$	−5.58 (−4.18)	1.40				
$n = \infty$	−5.52 (−4.50)		−4.99 (−3.98)		1.02 (1.01)	1.10[c]

[a] Values in parentheses are estimated band gaps of polymers in acetonitrile. [b] Reference 48. [c] Reference 13.

solution, and the deviation for $\mathbf{P_A}$ is larger than that of $\mathbf{P_C}$. The solvent effect may be an important factor that shifts the band edges relative to those in the gas phase, which will be discussed in the following.

Solvent Effects on Band Edges. As shown in Table 2 and Figure 3b, the further involvement of CH_3CN solvent molecules does cause the upshift of about 0.52 eV (0.53 eV) for the CB (VB) edge of $\mathbf{P_C}$ according to our combined DFT and MD calculations by using the explicit solvent model (with the computational details given in section 2). After considering the solvent effect, the calculated VB and CB of $\mathbf{P_C}$ are about −5.00 and −3.96 eV, respectively, in good agreement with the experimental data (−4.99 and −3.98 eV).

Interestingly, it is found from both PCM and explicit solvent models that only the HOMO−LUMO gap of $1\mathbf{P_C}$ in CH_3CN is subjected to the blue shift (see Table 2) due to the fact that the HOMO → LUMO transition is of $n \rightarrow \pi^*$ character, as shown in Figure S3 of the Supporting Information. In fact, such a solvent effect on the $n \rightarrow \pi^*$ transition has already been addressed.[38,46] However, in the case of longer $\boldsymbol{n}\mathbf{P_C}$ oligomers ($n > 1$), $\pi \rightarrow \pi^*$ becomes the dominant mode in the HOMO → LUMO transition, similar to that in $\boldsymbol{n}\mathbf{P_A}$; thus the HOMO−LUMO gaps of both $\boldsymbol{n}\mathbf{P_C}$ (when $n > 1$) and $\boldsymbol{n}\mathbf{P_A}$ undergo red shifts in CH_3CN.

Although the band shifts in CH_3CN solution are just estimated by simple solvent models due to the limitation of the present computational resource, the essence of the solvent effect in this kind of systems can still be qualitatively described without loss of generality. The polar side chains on the polyacetylene backbone generate a polarized field in the surrounding solvent, and in turn the polymer system is self-trapped in this polarized field. Influences of the charged side chains on the energy levels of frontier orbitals (and hence the band edges) of polyacetylene may be partly counteracted by this solvent effect.

PBC Calculations of Polymers. Band structures of $\mathbf{P_A}$ and $\mathbf{P_C}$, obtained by PBC/PW91 calculations, are shown in Figure 4. The VB and CB edges of $\mathbf{P_A}$ ($\mathbf{P_C}$) are −3.37 eV (−5.04 eV) and −2.27 eV (−4.22 eV), respectively. The band gap of 1.10 eV obtained by PBC calculation on $\mathbf{P_A}$ is in good agreement with that (1.09 eV) derived from the oligomer extrapolation scheme. The maximum deviation of band edges between these two methods is within 0.2 eV. For $\mathbf{P_C}$ the PBC calculation gives a band gap of 0.82 eV, slightly smaller than the value of 1.02 eV obtained via the oligomer extrapolation method. The larger deviations in band edges of $\mathbf{P_C}$ than those of $\mathbf{P_A}$ may be ascribed to the larger bending extent in the backbone of $\mathbf{P_C}$ (cf. Figure 1 and Figure S2). Thus, the values of band edges obtained from the oligomer extrapolation method are used in the following discussions.

3.3. Absence of the n-Doping Wave of $\mathbf{P_A}$. In spite of the downshift of about 0.54 eV (0.50 eV) for the CB (VB) edge of $\mathbf{P_A}$ (see Table 2 and Figure 3b) in the solvent of CH3CN, there is still a deviation of about 0.7 eV in the VB edge compared with the experimental determination. However, we notice that the voltammetry experiments[13] are carried out in the dilute 0.075 M Me_4NBF_4/CH_3CN solution. We assume that the influence of ionic atmosphere on the $-SO_3^-$ in the $-C_2H_4SO_3^-$ group is greatly larger than that on the $-N(Me)_3^+$ in the $-C_2H_4N(Me)_3^+$ group, since the radius of $-SO_3^-$ is smaller than that of $-N(Me)_3^+$. Therefore, the electrostatic screen of the ionic atmosphere of $-SO_3^-$ causes the further decrease of the electrostatic interaction between the $-C_2H_4SO_3^-$ group and the electrons on the valence band. As a result, the band edge of VB of the backbone of $\mathbf{P_A}$ drops to the vicinity of the experimental values.

We also notice that a transient feature in the voltamograms of $\mathbf{P_A}$ occurs upon driving to negative potentials of −1.0 V vs SCE, and this feature does not result in an electrically conductive

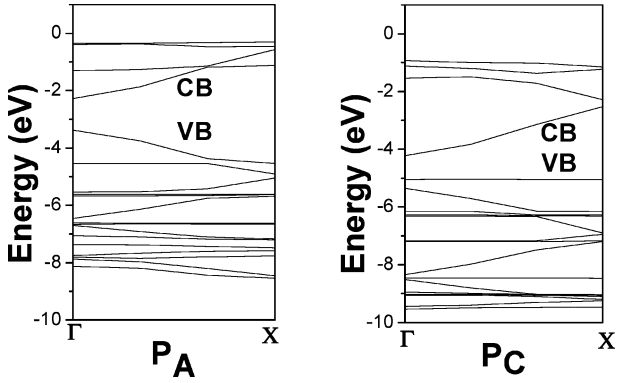

Figure 4. Band structures of $\mathbf{P_A}$ (left) and $\mathbf{P_C}$ (right) obtained from PBC/PW91 calculations (using the CASTEP program).

film of $\mathbf{P_A}$.[13] One possible reason may be that the ionic atmospheres near the $\mathbf{P_A}$/glass carbon electrode interface are polarized, and the local gathering of Me_4N^+ ions results in the capacitive electricity in the experiment. Subsequently, the CB of $\mathbf{P_A}$ near the interface indeed restores to that only in the solvent. As a result, only when the chemical potential of the glassy carbon electrode catches up with CB edge (about −2.17V vs SCE) can $\mathbf{P_A}$ be negatively doped in Me_4NBF_4/CH_3CN. Hence, it is not surprising that the n-doping wave is not observed experimentally when the bias is only reduced to −1.50V vs SCE.[8,13]

According to the transient feature at potentials of −1.00 V vs SCE, it is possible that there are large amount of $N(Me)_4^+$ accumulate at the $\mathbf{P_A}$/glass carbon interface region when the potential of the electrode is more negative than −1.00 V vs SCE. Hence, another reason why $\mathbf{P_A}$ cannot be n-doped may lie in that the carbon backbones of $\mathbf{P_A}$ are relatively far away from the glass carbon electrode under the negative scan condition, and the effective electron-transfer processes are broken down.

3.4. Charge Transfer and Transport. The interfacial charge transfer and transport in the Au|$\mathbf{P_C}$|$\mathbf{P_A}$|Au junction are surveyed from the relative energy levels of each component, the character of each buried interface after the electron-transfer process. In this work, the literature value of −5.31 eV[47] is taken as the Fermi level of the Au electrode.

$\mathbf{P_A}$|Au Interface. Because of the fact that the CB of $\mathbf{P_A}$ is higher than the Fermi energy level of Au electrode, electrons on the CB will transfer to the Au electrode, and an interfacial electric field forms finally. This field directs from $\mathbf{P_A}$ to the Au electrode because the injected holes accumulate at the interfacial region. Therefore, the CB in the bulk of $\mathbf{P_A}$ drops down until the Fermi energy level of $\mathbf{P_A}$ equals that of the Au electrode.

$\mathbf{P_C}$|$\mathbf{P_A}$ Interface. As shown in Figure 5, in shorter oligomers (when $n \leq 3$), the HOMO energy levels of $n\mathbf{P_A}$ are lower than the LUMO energy levels of $n\mathbf{P_C}$. When the oligomer size grows to $n = 4$, a transition in the relative positions of frontier orbitals of $n\mathbf{P_A}$ and $n\mathbf{P_C}$ occurs; i.e., the HOMO energy level (−3.63 eV) of $\mathbf{4P_A}$ is higher than the LUMO level (−3.84 eV) of $\mathbf{4P_C}$. Moreover, for the longer oligomers, the HOMO-1 energy levels of $\mathbf{7P_A}$ (−3.69 eV) and $\mathbf{8P_A}$ (−3.61 eV) are higher than the LUMO+1 energy levels of $\mathbf{7P_C}$ (−4.14 eV) and $\mathbf{8P_C}$ (−4.19 eV), respectively.

Thus, it seems that electrons can transfer at the interface between $\mathbf{P_A}$ and $\mathbf{P_C}$. After the electron-transfer process those released $N(CH_3)_4^+$ and $SO_3CF_3^-$ groups combine into ionic pairs of $N(CH_3)_4^+SO_3CF_3^-$ at the $\mathbf{P_C}$|$\mathbf{P_A}$ interface region. As discussed above, however, the interfacial electric field at the $\mathbf{P_A}$|Au interface results in the drop of band edge of $\mathbf{P_A}$. Finally, this

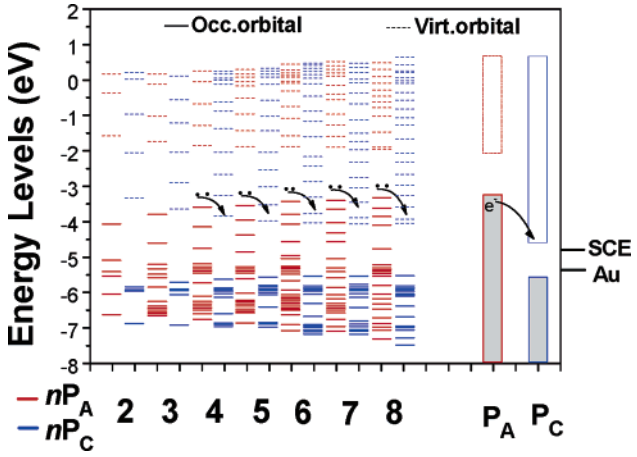

Figure 5. Energy levels of molecular orbitals of $n\mathbf{P_A}$ and $n\mathbf{P_C}$ oligomers ($n = 2-8$) and the extrapolated energy bands of $\mathbf{P_A}$ and $\mathbf{P_C}$ polymers relative to the saturated calomel electrode (SCE) and Au electrode.

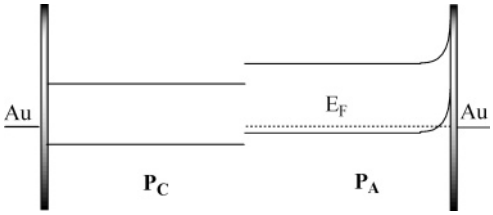

Figure 6. Schematic band diagram of the Au|$\mathbf{P_C}$|$\mathbf{P_A}$|Au junction, where E_F represents the unified Fermi energy level in the whole system.

electron-transfer process at the $\mathbf{P_C}$|$\mathbf{P_A}$ interface will carry out backward after the downshift of energy bands of $\mathbf{P_A}$. Here, one can see that the Au electrode at the $\mathbf{P_A}$|Au interface plays a dominant role in controlling the electronic properties of the Au|$\mathbf{P_C}$|$\mathbf{P_A}$|Au junction. It is reasonably anticipated that the electron-transfer process at the $\mathbf{P_C}$|$\mathbf{P_A}$ interface without the existence of Au electrode may generate the inner surface conducting phenomena as observed in the case of the surface doping of diamond.[24]

Energy Band Diagram. According to the above discussion of polymer/polymer and polymer/electrode interfaces, the band diagram of Au|$\mathbf{P_C}$|$\mathbf{P_A}$|Au junction after the process of electron transfer is schematically depicted in Figure 6, in which $\mathbf{P_A}$ has the same Fermi energy level as that of Au electrode.

Unidirectional Current. Actually, the Au|$\mathbf{P_C}$|$\mathbf{P_A}$|Au device is a two-layer LED. When it is subjected to a positive bias, holes injected from the $\mathbf{P_A}$|Au interface can overcome the energy barrier (with the height of about 0.20 eV) at the $\mathbf{P_C}$|$\mathbf{P_A}$ interface although the thickness of barrier is relatively large. Effective tunneling of holes from $\mathbf{P_A}$ to $\mathbf{P_C}$ can only occur at a smaller thickness of barrier, which can be realized by using a larger bias to tilt the energy band of $\mathbf{P_C}$. This process is consistent with the fact that the experimental onset bias for conduction of the device is about 0.90 eV. Note that no energy barrier exists for the injection of holes at the $\mathbf{P_A}$|Au interface. In contrast, there is an energy barrier of about 0.81 eV at the Au|$\mathbf{P_C}$ interface for the injection of electrons. Therefore, only holes in VB can function as the carriers. This transport process may involve only one kind of carrier, in agreement with the fact that there are no absorption spectra in experiment.[8]

Under the negative bias, the key factor that determines the transport behavior is the $\mathbf{P_A}$|Au interface rather than other interfaces. In this case, the holes in the $\mathbf{P_A}$|Au interfacial region resulting from electron-transfer process in the equilibrium device

are drawn out. Accordingly, the interfacial resistance enhances, causing the bias mainly dropping at this region. Since the applied bias does not generate the carriers, it cannot result in the conduction of the Au|$\mathbf{P_C}$|$\mathbf{P_A}$|Au system.

To summarize, we present an alternative picture on the basis of characteristics of both polymer/polymer and polymer/electrode interfaces to rationalize the intriguing experimental phenomena. Our calculation results supplement previous explanation from a view of ion polarization processes at Au|$\mathbf{P_C}$ and $\mathbf{P_A}$|Au interfaces.[8]

4. Conclusion

A theoretical description of the Au|$\mathbf{P_C}$|$\mathbf{P_A}$|Au junction has been presented on the basis of the relative energy levels of each component and the electronic structure of each buried interface in the device.

We use the DFT method and the linear scaling EC-MFCC strategy to optimize the ground-state geometries and calculate the energy levels of frontier orbitals of oligomers of the ionically functionalized $n\mathbf{P_A}$ and $n\mathbf{P_C}$ ($n = 1-8$). Both the oligomer extrapolation method and PBC calculations are adopted to obtain their energy gaps and band edges. The solvent effects on the band edges of $\mathbf{P_A}$ and $\mathbf{P_C}$ in the solvent of acetonitrile are also estimated by using both the PCM and explicit solvent model. According to the relative positions of the energy levels and the chemical potential of SCE, the absence of the n-doping wave in the voltammetry data of $\mathbf{P_A}$ is rationalized by its high reduction potential (−2.71V vs SCE in the gas phase and about −2.17V vs SCE in CH_3CN). Another reason may be that there are a large amount of $N(Me)_4^+$ accumulated at the $\mathbf{P_A}$/glass carbon interface region, making the carbon backbones relatively far away from the glass carbon electrode. When the Au|$\mathbf{P_C}$|$\mathbf{P_A}$|Au junction is under positive bias, holes injected from the $\mathbf{P_A}$|Au interface need to overcome the barrier of about 0.2 eV near the $\mathbf{P_C}$|$\mathbf{P_A}$ interface. Effective tunneling of holes from $\mathbf{P_A}$ to $\mathbf{P_C}$ can only occur at a smaller thickness of barrier, which can be realized by using a larger bias to tilt the energy band of $\mathbf{P_C}$. This process is consistent with the fact that the experimental onset bias for conduction of the device is about 0.90 eV. When the Au|$\mathbf{P_C}$|$\mathbf{P_A}$|Au junction is under the negative bias, the carrier cannot be generated in the VB of $\mathbf{P_A}$; in contrast, holes that injected in the equilibrium case are drawn out from the $\mathbf{P_A}$|Au interfacial region. The elucidation of unusual electronic and spectral properties of the Au|$\mathbf{P_C}$|$\mathbf{P_A}$|Au junction is essential to the development of ionomer-based microelectronic devices. Theoretical works toward quantitative descriptions of energy band diagram of this kind of junctions are still underway.

Acknowledgment. The authors thank five reviewers for their constructive and pertinent comments. This work is supported by the National Natural Science Foundation of China (Grants 20433020 and 20573050), the National Basic Research Program (Grant 2004CB719901), and the project from the Ministry of Education (NCET-05-0442).

Supporting Information Available: Details of the calculation with EC-MFCC approach (Figure S1); optimized geometries calculated with B3LYP/6-31g* of $n\mathbf{P_A}$ and $n\mathbf{P_C}$ ($n = 4-8$) (Figure S2); shift of HOMO−LUMO transition from the gas phase to solvent of acetonitrile and orbitals of HOMO and LUMO of $\mathbf{1P_C}$ and $\mathbf{1P_A}$ (Figure S3); complete ref 28 for Gaussian 03 program. This material is available free of charge via the Internet at http://pubs.acs.org.

References and Notes

(1) Pei, Q.; Yang, Y.; Yu, G.; Zhang, C.; Heeger, A. J. *J. Am. Chem. Soc.* **1996**, *118*, 3922.
(2) Pei, Q.; Yu, G.; Zhang, C.; Yang, Y.; Heeger, A. J. *Science* **1995**, *269*, 1086.
(3) deMello, J. C.; Tessler, N.; Graham, S. C.; Friend, R. H. *Phys. Rev. B* **1998**, *57*, 12951.
(4) Nilsson, D.; Chen, M.; Kugler, T.; Remonen, T.; Armgarth, M.; Berggren, M. *Adv. Mater.* **2002**, *14*, 51.
(5) Kittlesen, G. P.; White, H. S.; Wrighton, M. S. *J. Am. Chem. Soc.* **1985**, *107*, 7373.
(6) Ofer, D.; Crooks, R. M.; Wrighton, M. S. *J. Am. Chem. Soc.* **1990**, *112*, 7869.
(7) Chen, M.; Nilsson, D.; Kugler, T.; Berggren, M.; Remonen, T. *Appl. Phys. Lett.* **2002**, *81*, 2011.
(8) Cheng, C. H. W.; Boettcher, S. W.; Johnston, D. H.; Lonergan, M. C. *J. Am. Chem. Soc.* **2004**, *126*, 8666.
(9) Cheng, C. H. W.; Lonergan, M. C. *J. Am. Chem. Soc.* **2004**, *126*, 10536.
(10) Friend, R. H.; Gymer, R. W.; Holmes, A. B.; Burroughes, J. H.; Marks, R. N.; Taliani, C.; Bradley, D. D. C.; Santos, D. A. D.; Brédas, J. L.; Lögdlund, M.; Salaneck, W. R. *Nature (London)* **1999**, *397*, 121.
(11) Burroughes, D. D. C.; Brown, A. R.; Marks, R. N.; Mackay, K.; Friend, R. H.; Holmes, A. B. *Nature (London)* **1990**, *347*, 539.
(12) Braun, D.; Heeger, A. J. *Appl. Phys. Lett.* **1991**, *58*, 1982.
(13) Lonergan, M. C.; Cheng, C. H.; Langsdorf, B. L.; Zhou, X. *J. Am. Chem. Soc.* **2002**, *124*, 690.
(14) Langsdorf, B. L.; Zhou, X.; Adler, D. H.; Lonergan, M. C. *Macromolecules* **1999**, *32*, 2796.
(15) Langsdorf, B. L.; Zhou, X.; Lonergan, M. C. *Macromolecules* **2001**, *34*, 2450.
(16) Cheng, C. H. W.; Lin, F.; Lonergan, M. C. *J. Phys. Chem. B* **2005**, *109*, 10168.
(17) There are numerous theoretical works in this field. The list given below is far from complete. (a) Luo, Y.; Wang, C.-K.; Fu, Y. *J. Chem. Phys.* **2002**, *117*, 10283. (b) Luo, Y.; Wang, C.-K.; Fu, Y. *Chem. Phys. Lett.* **2003**, *369*, 299. (c) Jiang, J.; Kula, M.; Lu, W.; Luo, Y. *Nano Lett.* **2005**, *5*, 1551. (d) Zhao, J.; Zeng, C.; Cheng, X.; Wang, K.; Wang, G.; Yang, J.; Hou, J. G.; Zhou, Q. *Phys. Rev. Lett.* **2005**, *95*, 045502. (e) Kim, B.; Beebe, J. M.; Jun, Y.; Zhu, X.-Y.; Frisbie, C. D. *J. Am. Chem. Soc.* **2006**, *128*, 4970. (f) Li, Z.; Kosov, D. S. *J. Phys. Chem. B* **2006**, *110*, 9893. (g) Ke, S.-H.; Baranger, H. U.; Yang, W. *J. Am. Chem. Soc.* **2004**, *126*, 15897. (h) Xue, Y.; Datta, S.; Ratner, M. A. *Chem. Phys.* **2002**, *281*, 151. (i) Damle, P. S.; Ghosh, A. W.; Datta, S. *Phys. Rev. B* **2001**, *64*, 201403. (j) Tada, T.; Nozaki, D.; Kondo, M.; Hamayama, S.; Yoshizawa, K. *J. Am. Chem. Soc.* **2004**, *126*, 14182. (k) Jiang, F.; Zhou, Y. X.; Chen, H.; Note, R.; Mizuseki, H.; Kawazoe, Y. *Phys. Rev. B* **2005**, *72*, 155408.
(18) Hu, W.; Jiang, J.; Nakashima, H.; Luo, Y,; Kashimura, Y.; Chen, K.-Q.; Shuai, Z.; Furukawa, K.; Lu, W.; Liu, Y.; Zhu, D.; Torimitsu, K. *Phys. Rev. Lett.* **2006**, *96*, 027801.
(19) (a) Yang, W. *Phys. Rev. Lett.* **1991**, *66*, 1438. (b) Yang, W.; Lee, T.-S. *J. Chem. Phys.* **1995**, *103*, 5674. (c) Lee, T.-S.; York, D. M.; Yang, W. *J. Chem. Phys.* **1996**, *105*, 2744.
(20) (a) Exner, T. E.; Mezey, P. G. *J. Phys. Chem. A* **2002**, *106*, 11791. (b) Exner, T. E.; Mezey, P. G. *J. Comput. Chem.* **2003**, *24*, 1980. (c) Exner, T. E.; Mezey, P. G. *J. Phys. Chem. A* **2004**, *108*, 4301.
(21) (a) Zhang, D. W.; Zhang, J. Z. H. *J. Chem. Phys.* **2003**, *119*, 3599. (b) Zhang, D. W.; Xiang, Y.; Zhang, J. Z. H. *J. Phys. Chem. B* **2003**, *107*, 12039.
(22) (a) Kitaura, K.; Ikeo, E.; Asada, T.; Nakano, T.; Uebayasi, M. *Chem. Phys. Lett.* **1999**, *313*, 701. (b) Kitaura, K.; Sugiki, S.-I.; Nakano, T.; Komeiji, Y.; Uebayasi, M. *Chem. Phys. Lett.* **2001**, *336*, 163. (c) Fedorov, D. G.; Kitaura, K. *J. Chem. Phys.* **2004**, *120*, 6832. (d) Fedorov. D. G.; Kitaura, K. *Chem. Phys. Lett.* **2004**, *389*, 129.
(23) Li, S.; Li, W.; Fang, T. *J. Am. Chem. Soc.* **2005**, *127*, 7215.
(24) (a) Ristein, J. *J. Phys. D: Appl. Phys.* **2006**, *39*, R71. (b) Zhang, P.; Tevaarwerk, E.; Park, B.-N.; Savage, D. E.; Celler, G. K.; Knezevic, I.; Evans, P. G.; Eriksson, M. A.; Lagally, M. G. *Nature (London)* **2006**, *439*, 703.
(25) Becke, A. D. *J. Chem. Phys.* **1993**, *98*, 5648.
(26) Becke, A. D.; Roussel, M. R. *Phys. Rev. A* **1989**, *39*, 3761.
(27) Lee, C.; Yang, W.; Parr, R. G. *Phys. Rev. B* **1988**, *37*, 785.
(28) Frisch, M. J.; et al. *Gaussian 03*, Revision B.04; Gaussian, Inc.: Pittsburgh, PA, 2003.
(29) Salzner, U.; Lagowski, J. B.; Pickup, P. G.; Poirier, R. A. *Synth. Met.* **1998**, *96*, 177.
(30) Ma, J.; Li, S.; Jiang, Y. *Macromolecules* **2002**, *35*, 1109.
(31) Yang, S.; Olishevski, P.; Kertesz, M. *Synth. Met.* **2004**, *141*, 171.
(32) Cao, H.; Ma, J.; Zhang, G.; Jiang, Y. *Macromolecules* **2005**, *38*, 1123.
(33) *Cerius*^{2}, Molecular Simulation Inc., version 3.5, 1997.

(34) There are numerous works in studies of solvent effects. We only choose some reviews and representative works here. The list given here is far from complete. (a) Cramer, C. J.; Truhlar, D. G. *Chem. Rev.* **1999**, *99*, 2161. (b) Orozco, M.; Luque, F. J. *Chem. Rev.* **2000**, *100*, 4187. (c) Tomasi, J.; Mennucci, B.; Cammi, R. *Chem. Rev.* **2005**, *105*, 2999. (d) Barone, V.; Cossi, M.; Tomasi, J. *J. Comput. Chem.* **1998**, *19*, 404. (e) Gao, J.; Alhambra, C. *J. Am. Chem. Soc.* **1997**, *119*, 2962. (f) Cabral do Couto, P.; Estácio, S. G.; Costa Cabral, J. *J. Chem. Phys.* **2005**, *123*, 054510.

(35) Allen, M. P.; Tildesley, D. J. *Computational Simulation of Liquids*; Oxford: New York, 1987.

(36) There are many theoretical works on **PA**, e.g.: (a) Su. W. P.; Schrieffer, J. R.; Heeger, J. *Phys. Rev. Lett.* **1979**, *42*, 1698. (b) Su. W. P.; Schrieffer, J. R.; Heeger, A. J. *Phys. Rev. B* **1980**, *22*, 2099. (c) Kivelson, S. *Phys. Rev. Lett.* **1981**, *46*, 1344. (d) Kivelson, S. *Phys. Rev. B* **1982**, *25*, 3798. (e) Yamabe, T.; Tanaka, K.; Yamanaka, S.; Koike, T.; Fukui, K. *J. Chem. Phys.* **1985**, *82*, 5737. (f) Zhao, C.; Sun, Y.; Wang, R. *Acta Chim. Sin.* **1986**, *4*, 348. (g) Ma, H.; Liu, C.; Jiang, Y. *J. Chem. Phys.* **2004**, *120*, 9316; **2005**, *122*, 104909; **2005**, *123*, 084303.

(37) Ito, T.; Shirakawa, H.; Ikeda, S. *J. Polym. Sci., Chem. Ed.* **1974**, *12*, 11.

(38) Chiang, C. K.; Park, Y. W.; Heeger, A. J.; Shirakawa, H.; Louis, E. J.; MacDiarmid, A. G. *Phys. Rev. Lett.* **1977**, *39*, 1098.

(39) Debye, P. P.; Conwell, E. M. *Phys. Rev.* **1954**, *93*, 693.

(40) Lee, T. F.; McGill, T. C. *J. Appl. Phys.* **1975**, *46*, 373.

(41) Fontaine, F. *J. Appl. Phys.* **1999**, *85*, 1409.

(42) Suzuki, S.; Maeda, F.; Watanabe, Y.; Ogino, T. *Phys. Rev. B* **2003**, *67*, 115418.

(43) Salzner, U. *Synth. Met.* **2001**, *119*, 215.

(44) Roncali, J. *Chem. Rev.* **1997**, *97*, 173.

(45) Reiss, H.; Heller, A. *J. Phys. Chem.* **1985**, *89*, 4207.

(46) Bayliss, N. S.; McRae, E. G. *J. Phys. Chem.* **1954**, *58*, 1002.

(47) *CRC Handbook of Chemistry and Physics*, 81st ed.; Lide, D. R., Ed.; CRC Press: Boca Raton, FL, 2000; pp 12−130.

(48) Tani, T.; Grant, P. M.; Gill, W. D.; Street, G. B.; Clarke, T. C. *Solid State Commun.* **1980**, *33*, 499.

MA0703857